

# Experimental Project Report - Exploration of paraelectric properties for tunable antennas

Corwin Shiu

Adviser: Professor Bill Jones

November 1, 2017

## Contents

<b>1</b>	<b>Motivation</b>	<b>1</b>
<b>2</b>	<b>Approach, modeling and literature review</b>	<b>2</b>
2.1	Devonshire's model of ferroelectrics . . . . .	2
2.2	Existing material measurements . . . . .	3
<b>3</b>	<b>Dielectric Measurement Theory</b>	<b>5</b>
3.1	Two port unbiased measurement . . . . .	5
3.2	Resonant Cavity measurement of $\epsilon_r$ . . . . .	8
<b>4</b>	<b>Antenna Concept</b>	<b>15</b>
<b>5</b>	<b>Hardware modifications for a 4K measurement of dielectric properties</b>	<b>16</b>
<b>6</b>	<b>Future Work</b>	<b>18</b>

## 1 Motivation

**CMB Foregrounds.** A detection of the B-mode polarization of the Cosmic Microwave Background (CMB) would be a measurement of a cosmological gravitational wave background. This measurement is difficult because it is expected to be a weak signal with large astrophysical foregrounds. Polarized CMB foregrounds must be carefully subtracted out to recover the underlying primordial gravitational wave signal.

Electrons gyrating in galactic magnetic fields produce synchrotron radiation up to 70 GHz. At higher frequencies, thermal emission from magnetically aligned dust particles contaminate our signal. We need to observe at many different frequencies to fully characterize these foregrounds.

**SPIDER experiment.** SPIDER is a balloon-borne CMB camera optimized for the inflationary CMB polarization signal. It has six cryogenically cooled, polarized mm-wave cameras with an angular degree resolution. Its inaugural flight in 2015 produced 10% sky maps at 95GHz and 150GHz. Second flight of SPIDER with target launch date of 2018 will have two, 285GHz cameras designed to target polarized dust emission.

**Motivation for research project.** All CMB polarimetry experiments need to observe at several frequencies for foreground subtraction. Different collaborations employ different methods. SPIDER and BICEP/Keck Array style cameras are single color, but deploy several different frequency cameras in the full telescope. Simons Array and South Pole Telescope (SPT) have developed wide band antennas and feedhorns which use band defining filters to create bands at 95, 150 and 220 GHz.

The motivation for this experimental project is to explore the feasibility of a frequency tunable antenna, so that we are able to create one camera which can be continuously tuned to the desired band of observation. This would allow us to observe the CMB at fine frequency bands to fully characterize both the synchrotron radiation and polarized galactic dust spectrum and to refine both aspects of foreground subtraction.

## 2 Approach, modeling and literature review

Frequency tunability can be accomplished either from having a wideband antenna with an electrically tunable filter or tuning the electrical length of a resonant antenna. Because the physical length cannot be changed with antennas defined by lithography, tunable material properties are the only path forward. CMB detectors are cryogenically cooled, so relevant material properties must be at  $\sim 300\text{mK}$ . In addition, CMB cameras operate at very high frequencies (150GHz), so measurements that are relevant are far and few between.

An electronically tunable ferroelectric is an ideal candidate. By building an antenna on top of such an material, when we tune the polarizability of the material, we tune the resonant frequency of the antenna.

### 2.1 Devonshire's model of ferroelectrics

Devonshire's phenomenological theory has been very successful in explaining common ferroelectrics, and serves as a launch point for understanding material properties. The free energy density is the thermodynamic energy available in a ferroelectric to do work, and can be written as an even power expansion of polarizability [6],

$$G = G_0 + \beta(T - T_0)P^2 - BP^4 + CP^6 \quad (1)$$

where  $G_0$  is the free energy for zero polarization, the  $\beta(T - T_0)$  coefficient is in linear proportion to temperature and  $C, B$  are coefficients. Higher order terms are omitted. Odd powers of polarization are omitted because reversal in direction of polarization should not change the free energy. The electric field can be found by differentiating free energy with  $P$ ,

$$E = 2\beta(T - T_0)P - 4BP^3 + 6CP^5$$

so for small  $P$  in the paraelectric regime higher order terms disappear, leaving  $E = 2\beta(T - T_0)P$ . Its easy to differentiate the equation to get dielectric constant,

$$\epsilon = \frac{\partial P}{\partial E} = \frac{1}{2\beta(T - T_0)} \quad (2)$$

which recovers the Curie-Weiss law [4], with a Curie coefficient of  $1/2\beta$  and Curie Weiss temperature  $T_0$ . As the material is cooled from  $T > T_0$  to  $T = T_0$ , the dielectric constant goes to infinity. Many other properties can be computed from this free-energy model, but for the rest of the document, they are not particularly relevant so we will omit them.

## 2.2 Existing material measurements

The discovery paper by Burkard and Muller measured the dielectric constant of strontium titanate (SrTiO<sub>3</sub> or STO from here) and showed that the material behaves like a classical paraelectric as described by equation 2, but never reaches the Curie point [3]. The material remains in a stable paraelectric phase at temperatures below 4K. CMB cameras operate at these temperatures, so this material would be advantageous for the two reasons

- (i) Paraelectric phase is advantageous over a ferroelectric phase when we desire a continuously tunable antenna. Hysteresis of the material would complicate operation because it is inherently non-linear.
- (ii) Stable dielectric constant below 4K is advantageous in reducing instrument systematics. In a real operating system, temperature gradients exist our focal plane. The stability of STO below 4K naturally prevents frequency drifting.

The paper did not measure the tunability of the material, or the dielectric constant at our frequencies of interest.

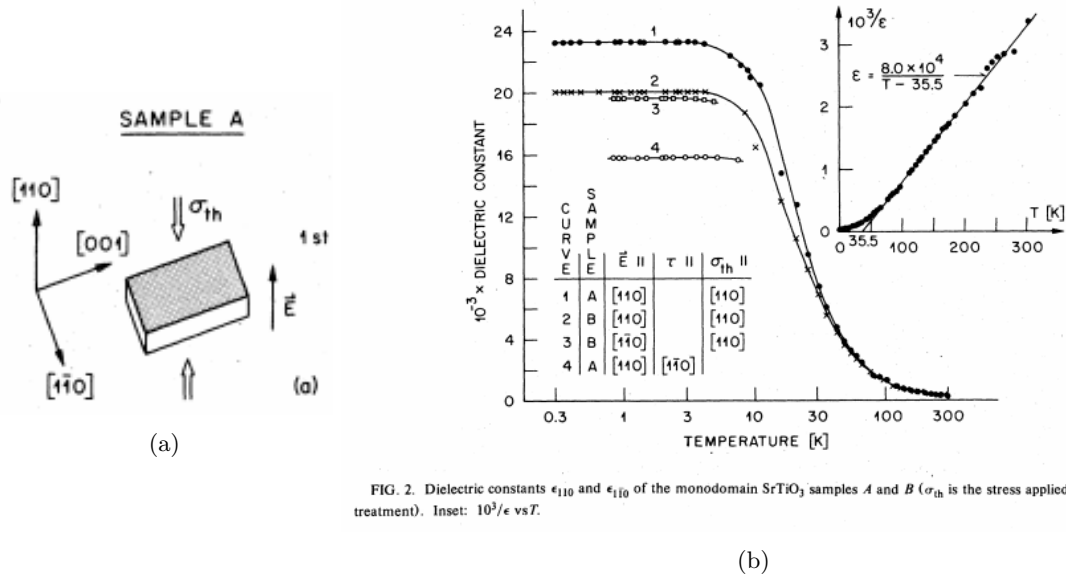


FIG. 2. Dielectric constants  $\epsilon_{110}$  and  $\epsilon_{110}$  of the monodomain  $\text{SrTiO}_3$  samples *A* and *B* ( $\sigma_{th}$  is the stress applied by thermal treatment). Inset:  $10^3/\epsilon$  vs  $T$ .

Figure 1: (a) Measurement setup. Hashed fill shows electrodes forming a parallel plate capacitor, and  $\sigma_{th}$  shows the application of thermal stress. The capacitance value was measured through a 3-port AC capacitance bridge. (b) Dielectric constant of  $\text{SrTiO}_3$  in paper [3].  $\text{SrTiO}_3$  samples were under different bias fields and stresses - all samples show the behavior of approaching a ferroelectric transition near 4K, and then stabilizing.

A recent paper(May 2017) showed tunability of the STO at 4K. They fabricated a superconducting CPW resonator on top of a STO substrate, and measured the reflection of the resonator as as they DC biased the CPW line [7]. Figure 2 shows the experimental setup and measurement results. As a DC bias voltage is applied from the CPW to ground, the resonant peaks of the CPW resonator shifts in frequency, indicating that the dielectric constant changes. This demonstrates the proof of principle behind the operation of a tunable antenna. However, the measured values are not portable to our experiment. The dielectric constant at 100s of MHz will be significantly different than 100s of GHz due to the underlying micro-scale physics behind polarizability.

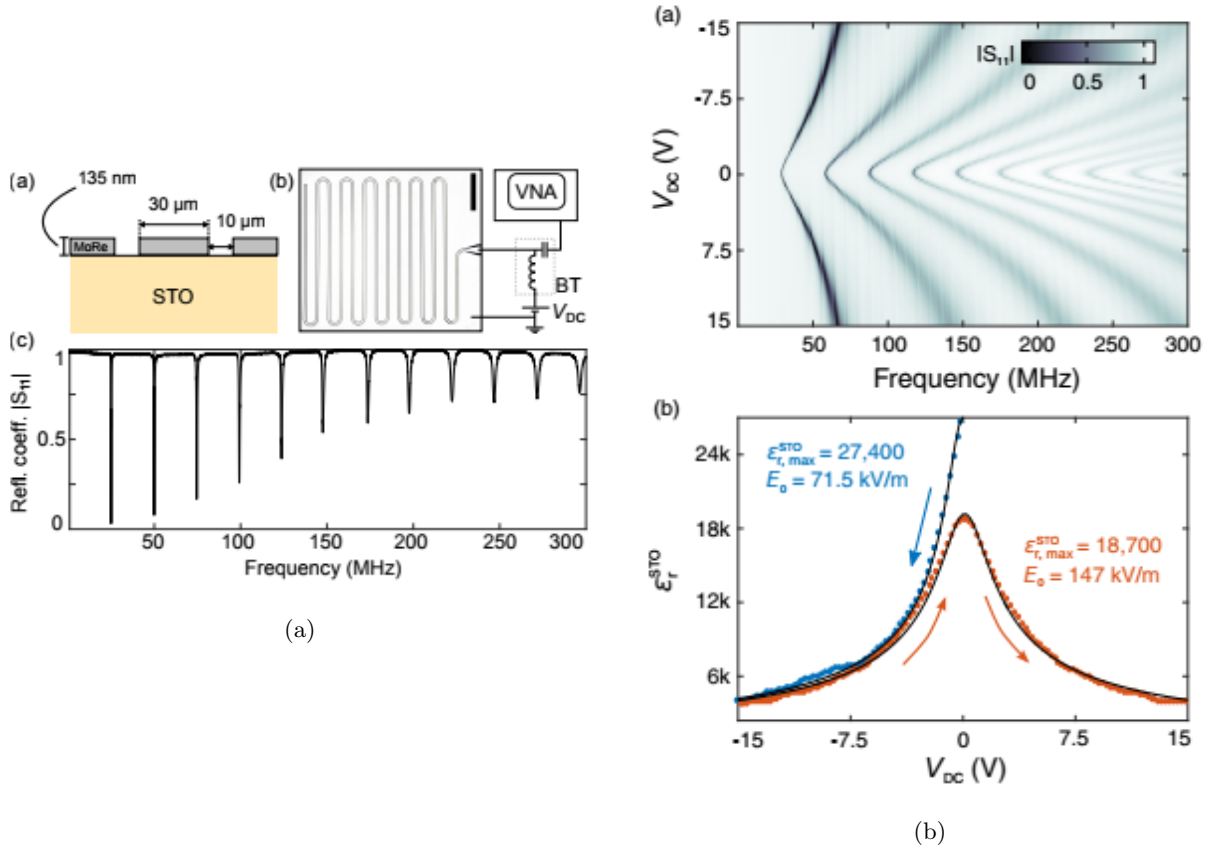


Figure 2: (a) shows the experimental setup. A VNA probes the reflection of a CPW resonator, which is biased directly. (b) shows the tunability of the resonant peaks by biasing the dielectric sample.

### 3 Dielectric Measurement Theory

We need to measure the properties of STO under the operating conditions seen in all CMB telescopes - low temperatures of  $\sim 300\text{mK}$  and at frequencies of  $\sim 150\text{GHz}$ . In particular we want to know, the dielectric constant  $\epsilon_r$  and the loss tangent  $\tan \delta$  as functions of bias voltage of our sample.

At Princeton, in Dr. Norm Jarosik's laboratory, we have a Heward Packartt 8510c Vector Network Analyzer. It is outfitted with a 85105A mm wave controller that houses the RF, LO, and IF amplifiers and switches required for operation. The input and output is connected with a pair of W85104A test set modules to get WR10 input and outputs to the VNA.

#### 3.1 Two port unbiased measurement

Strontium titanate was ordered from Princeton Scientific. In particular we acquired a 0.5mm thick, 5mm  $\times$  5mm sample.

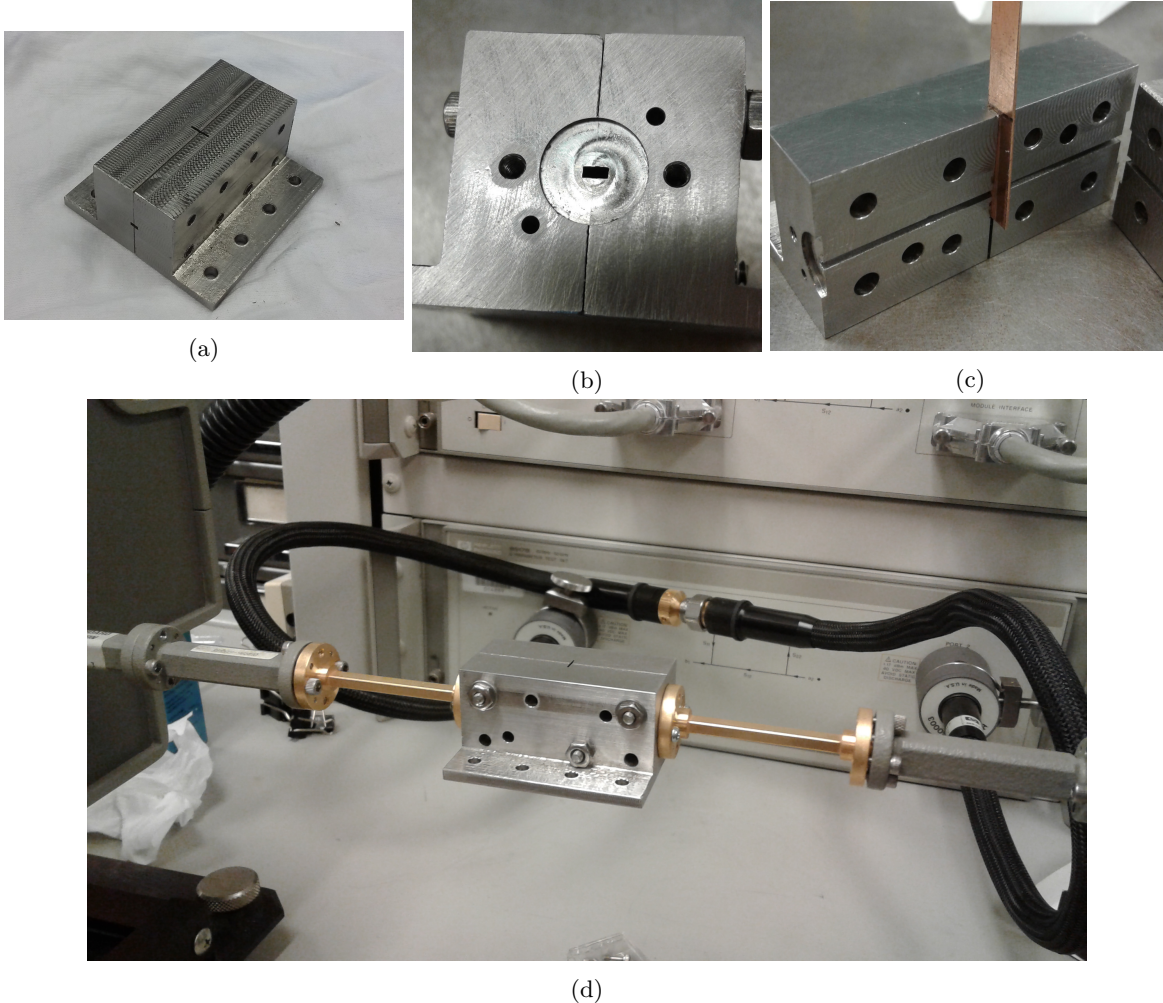


Figure 3: (a) shows the two pieces of the splitblock. (b) shows a flange pattern that we machined onto the face. (c) shows the inside of the splitblock, with a copper shim stock that has the same thickness and width of our dielectric sample. Although it appears the cut extends to the bottom of the waveguide block, this is an artifact of the machining process. A  $5\text{mm} \times 5\text{mm}$  substrate would not be able to slide through. (d) shows our splitblock attached for the VNA measurement.

We machined a WR10 split-block waveguide with a vertical slot that allowed the dielectric to be slipped to block the cross section as shown in figure 3. This method allowed for a non-destructive test of a STO substrate.

Power propagates down as a  $\text{TE}_{10}$  mode in a rectangular waveguide, until it meets a dielectric interface. It is then reflected back to the port or scatters into plane-waves in the dielectric. It then meets a second interface where it is reflected back (forming a resonant cavity), or transmitted through. The full field analysis of this geometry would allow us to back out the  $\epsilon(\omega)$ , but the full analysis is difficult and not particularly insightful. In addition, EM simulation software like CST or HFSS is inadequate when dealing with large dielectric constants - a lot of computing power must be used to handle very fine meshes at dielectric boundaries.

Instead transmission line theory can vastly simplify the analysis.

The waves propagating in the dielectric are TEM-plane waves, so the wave impedance looking into the dielectric is [5],

$$Z_{in} = Z_0 \frac{Z_L + jZ_0 \tan(\beta\ell)}{Z_0 + jZ_L \tan(\beta\ell)} \quad (3)$$

where  $Z_0 = \sqrt{\mu/\epsilon}$  is the characteristic impedance of the dielectric,  $\beta\ell$  is the electrical length of the dielectric and  $Z_L$  is the load impedance. When the dielectric slab is an integer multiple of  $\lambda/2$  then  $\beta\ell = n\pi$ , so the impedance seen into the dielectric is transformed away,

$$Z_{in}(\beta\ell = n\pi) = Z_L$$

physically this occurs because we have destructive interference of the reflected wave at the waveguide-dielectric junction. We get a peak in transmission and a dip in reflection.

### Measurement results

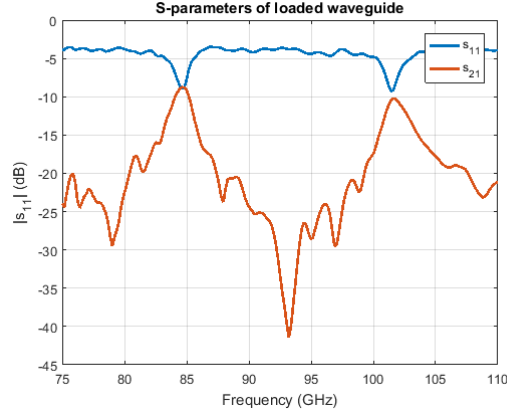


Figure 4: Reflection and transmission with our dielectric sample in the cavity.

The two resonant features in band occurs at,

$$f_0 = 84.63 \pm 0.175GHz, \quad f_0 = 101.6 \pm 0.175GHz$$

corresponding to,

$$\Delta f = 16.97 \pm 0.175GHz$$

These resonant peaks are multiplies of half-wavelengths so  $\Delta f$  corresponds to  $L = \lambda/2$ . This allows us to

calculate the electric constant in the medium,

$$\Delta f \times 2L = \frac{c}{\sqrt{\epsilon_r}}, \quad \Rightarrow \quad \epsilon = \left( \frac{c}{\Delta f \cdot 2L} \right)^2$$

and we get,

$$\boxed{\epsilon_r = 312.5 \pm 6.4} \tag{4}$$

The power loss in principle probes the dielectric loss tangent of the material. However we suspect the results are not going to be accurate. We suspect that we have much higher conductive loss than textbook expressions for waveguide components - due to poor finishes inside of the machined waveguides, air gaps and misalignment between waveguide components. All of these imperfections are apparent when we compare full EM-wave simulations with measurements.

### 3.2 Resonant Cavity measurement of $\epsilon_r$

The reflection transmission measurement of  $\epsilon_r$  gave us a first look, but is inadequate. We are unable to bias the sample to measure how the dielectric responds to an applied electric field. We are forced to use a resonant cavity and measure how the resonances tune.

**Perturbation method** Traditionally a dielectric is placed in a resonant cavity which will shift the cavity resonances. If the dielectric is both small and the dielectric constant is small, the fractional change of the resonant frequency can be approximated by [5],

$$\frac{\omega - \omega_0}{\omega} \simeq - \frac{\int_{V_0} (\Delta\epsilon |\vec{E}_0|^2 + \Delta\mu |\vec{H}_0|^2) dv}{\int_{V_0} (\epsilon |\vec{E}_0|^2 + \mu |\vec{H}_0|^2) dv} \tag{5}$$

where  $\vec{E}_0, \vec{H}_0$  are the unperturbed E and H fields of the cavity and  $\Delta\epsilon, \Delta\mu$  is the change in the dielectric and magnetic permeability at a point in space caused by the material. The small dielectric approximation is *not* valid in our scenario with  $\epsilon_r \approx 300$  at W-band frequencies. High dielectric constants modify the fields in the cavity so the perturbed fields do not look like the original modes.

#### Symmetrically loaded rectangular waveguide

Because the full field analysis is both difficult and not particularly enlightening, we can use a different procedure to find resonant modes. We use the transverse resonance procedure outlined in both [5], [1] to compute the resonant modes. The physical motivation behind why the procedure works is to enforce a standing wave in the direction transverse to the mode propagation.

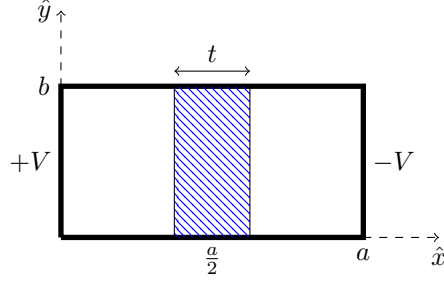


Figure 5: Cross section of a partially filled waveguide geometry, with the bias method.

A uniform waveguide will always have the mode propagation constant  $\beta$ ,

$$\beta = \sqrt{k^2 - k_c^2}$$

where  $k$  is the free-space propagation and  $k_c$  is the cutoff of the mode. In this particular case, we have two expressions coming from the air region and the dielectric region in the waveguide,

$$\beta = \sqrt{k_0^2 - k_a^2 - \left(\frac{m\pi}{b}\right)^2} \quad (6)$$

$$\beta = \sqrt{\epsilon_r^2 k_0^2 - k_d^2 - \left(\frac{m\pi}{b}\right)^2} \quad (7)$$

where  $k_a$  is the wavenumber in air,  $k_d$  is the wavenumber in the dielectric, and the  $m\pi/b$  wavenumber of the  $m$ -th mode in the  $y$  direction. By definition of a normal mode, the propagation constant  $\beta$  is the same between the two media, so equations 6 and 7 set up a constrain equation.

We can then apply the transverse equivalent transmission line circuit, shown in figure 6a. However even this produces an unwieldy equation to use. We can instead exploit symmetry, by breaking the modes into anti-symmetric and symmetric parts as shown in figure 6b.

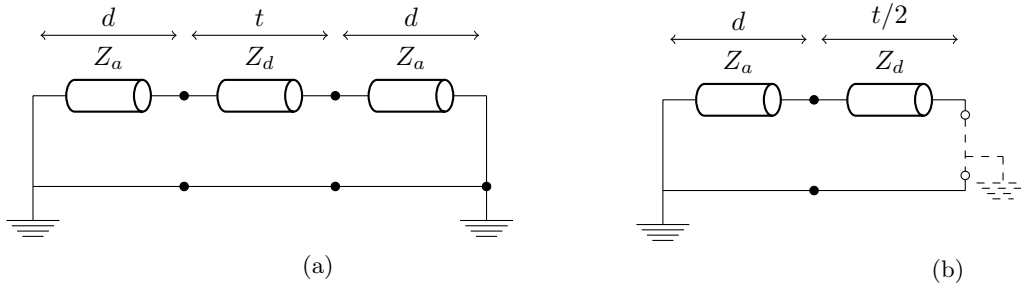


Figure 6: (a) Transverse equivalent transmission-line circuit. (b) Applying symmetry to the circuit model. We can have an open (symmetric) or a short (antisymmetric) across the dielectric.

Rectangular waveguide modes relate impedance to wavenumber,

$$Z_a \propto \frac{1}{k_a} \quad (8)$$

$$Z_d \propto \frac{1}{k_d} \quad (9)$$

For a symmetric mode, we have an open across the junction. The input impedance looking towards the right at  $x = d$  is computed the same way,

$$Z_{in}(x = d) = \frac{Z_d}{j \tan k_d \frac{t}{2}} = -j Z_d \cot k_d \frac{t}{2}$$

and the input impedance at  $x = 0$  is,

$$Z_{in}(x = 0) = Z_a \frac{-j Z_d \cot k_d \frac{t}{2} + j Z_a \tan k_a d}{Z_a + Z_a Z_d \cot k_d \frac{t}{2} \tan k_a d}$$

which must equal zero, so we are left with the constraint,

$$k_a \cot k_d \frac{t}{2} = k_d \tan k_a d \quad (10)$$

For the antisymmetric mode, we have a short across the junction. Omitting the steps because they are identical in detail, gives us the constraint equation,

$$k_a \tan k_d \frac{t}{2} = -k_d \tan k_a d \quad (11)$$

We can numerically solve the transcendental equation to find the propagating modes. For a silicon slab in a WR10 cavity, we compute the lowest order modes and their wavespeed at each frequency shown in figure 7a, which we can compare with HFSS in figures 7b and 7c.

Figure 7c shows we expect three features in our measurement band, but that we have poor predictability of the resonant frequencies from the analytic treatment. This occurs because of the presence of the coupling aperture. Near field E-fields are not well matched to the box modes E-fields for the first and third mode, resulting in a deviation from the analytic treatment. Simulated fields are shown in figure and even by visual inspect we see a departure from an idealized mode.

The drawbacks to this method shows that measuring even large dielectric constants would be difficult. We run the analytic methods and find that in the same 50 mil, WR10 cavity would have the modal structure in figure 9. We have 17 features of the type  $LSE_{m0\ell}$ . Modes will overlap and untangling modes become an

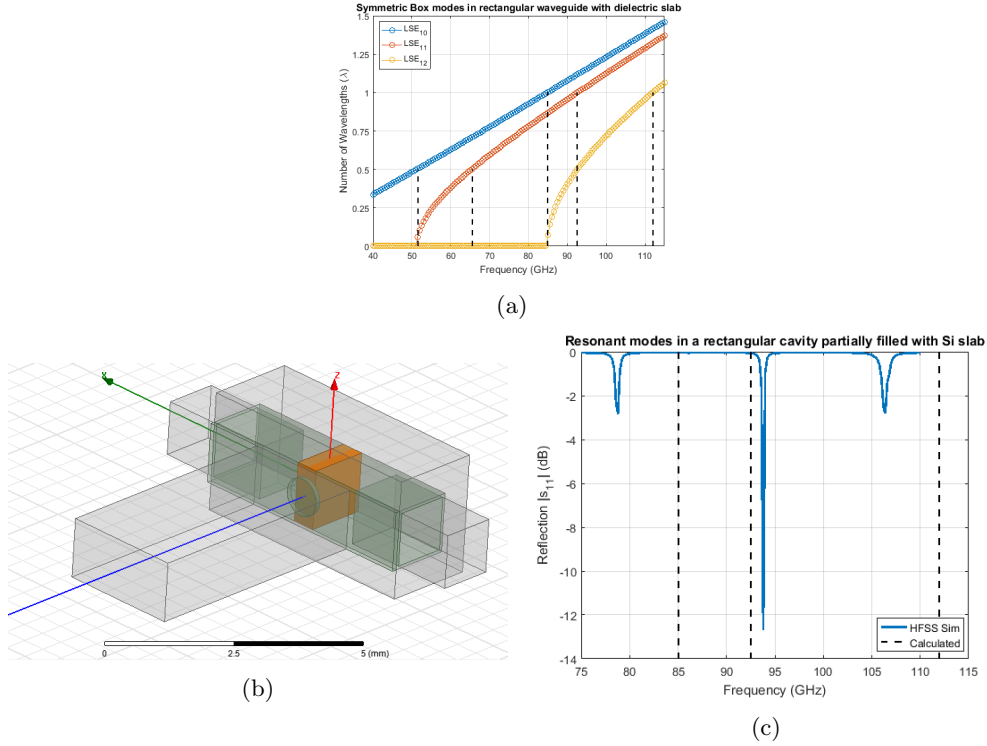


Figure 7: (a) Resonant modes in a WR10 waveguide box of length 0.05in, with a vertically oriented silicon slab as shown in figure 7b. The slab has dimensions 50 mils square and 0.5mm thick. (b) shows the simulation geometry of a realistically machined waveguide cavity. We have a rectangular cavity with a silicon slab (orange) oriented vertically with floating sidewalls. (c) The resonant modes of the box, with the expected resonances from analytical calculation. We have significant differences for the LSE102 and LSE122 resonant modes because of the coupling aperture.

impossible task. This method would not provide a clean measurement of our dielectric sample.

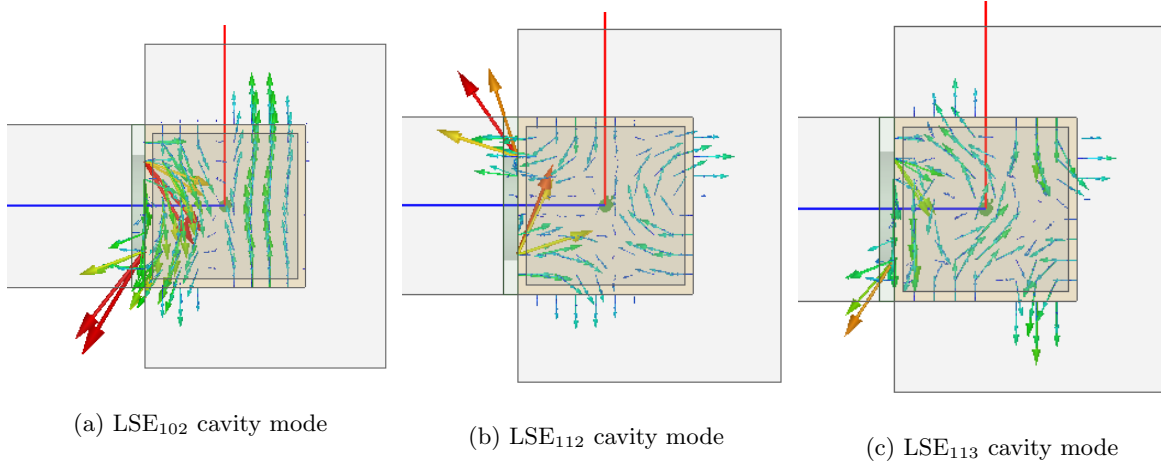


Figure 8: Low order cavity modes, with the presence of the coupling aperture. Fields in (a) and (c) are particularly modified due to the presence of the aperture.

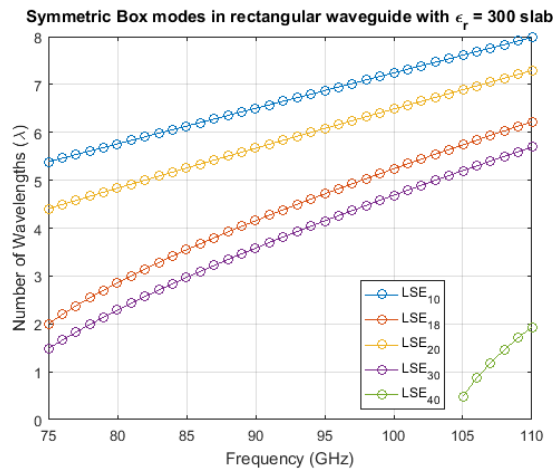


Figure 9: Modal structure of a high dielectric  $\epsilon_r = 300$  slab in a rectangular waveguide with geometric values identical to figure 7b. Even though we only plot  $LSE_{m0\ell}$  modes, we have 17 features in our measurement band. We can easily see that this method is unsuitable for high dielectric constants.

### Transverse loaded rectangular waveguide

Another potential resonant cavity is shown in figure 10. Once again, a full field analysis is difficult and not enlightening. We can use transmission line theory - only looking at one mode of the system - and break the system into three parts: two waveguides with no dielectric and a waveguide filled with dielectric. Using the same procedure as the transverse resonance method, we get the transcendental equation,

$$2 \frac{Z'}{Z} \tan \beta \ell_1 + \left( \frac{Z'}{Z} \right)^2 \tan \beta' \ell_2 = \tan^2 \beta \ell_1 \tan \beta_2 \ell_2 \quad (12)$$

where  $\ell_1, \ell_2$  are the lengths of the rectangular waveguide with vacuum and dielectric respectively,  $\beta, \beta'$  are the wavenumbers in each respectively, and  $Z, Z'$  are the wave impedance in each separately. The wavenumbers

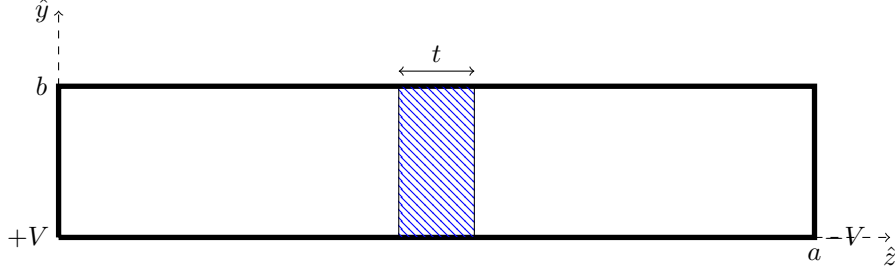


Figure 10: Cross section of a partially filled waveguide geometry.

are the usual rectangular waveguide ones,

$$\beta = \sqrt{\left(\frac{2\pi f}{c}\right)^2 - \left(\frac{\pi}{a}\right)^2} \quad (13)$$

$$\beta' = \sqrt{\left(\frac{2\pi f \sqrt{\epsilon_r}}{c}\right)^2 - \left(\frac{\pi}{a}\right)^2} \quad (14)$$

The ratio of the impedances is,

$$\frac{Z'}{Z} = \frac{k' \eta' \beta}{\beta' k \eta} = \frac{k' \eta' \beta}{k \eta \beta'} = \sqrt{\frac{\left(\frac{2\pi f}{c}\right)^2 - \left(\frac{\pi}{a}\right)^2}{\left(\frac{2\pi f \sqrt{\epsilon_r}}{c}\right)^2 - \left(\frac{\pi}{a}\right)^2}} \quad (15)$$

where the  $k'/k$  gives a factor of  $\sqrt{\epsilon_r}$  and ratio of the free space impedance is  $\eta'/\eta = 1/\sqrt{\epsilon_r}$  so they cancel. The results are shown in figure 11 which show great agreement between EM simulations and our analytic treatment. The resonant peaks are uniformly tuned away from the analytic model due to the effects of the coupling aperture. The simplifying assumption that we only have propagating modes of type  $TE_{10}$  is well satisfied seeing the simulated results.

We can perform the same analysis with a high dielectric constant, which is shown in figure 12. The frequency resolution of our Network analyzer is 0.176GHz, which will be fine enough to resolve the differences in these peaks.

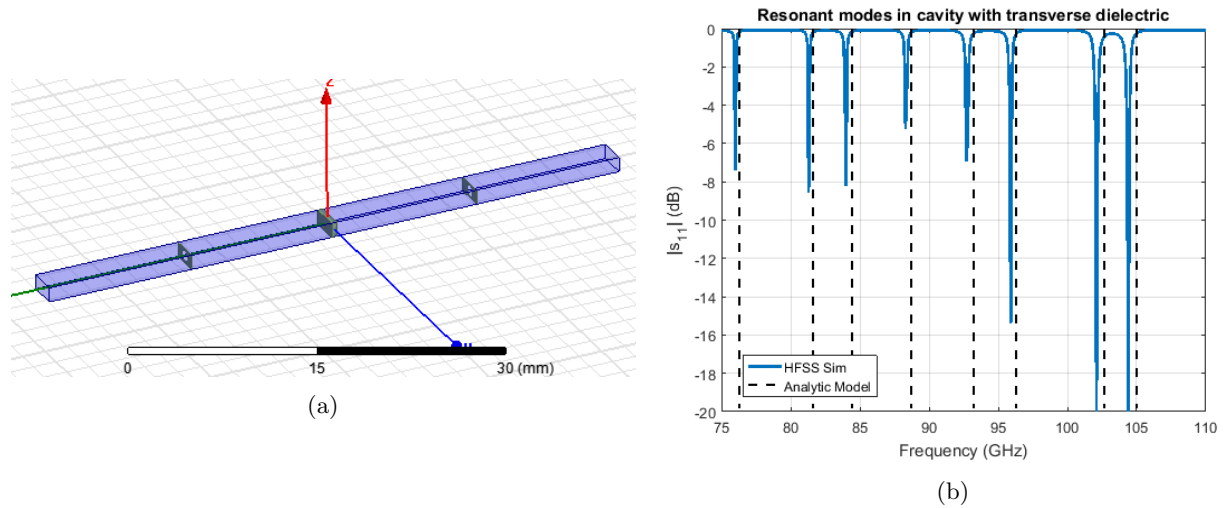


Figure 11: (a) shows the simulation geometry, with a transverse silicon slab in a waveguide with two coupling apertures. (b) shows both simulated reflection and analytically computed peaks. We good agreement between the peaks.

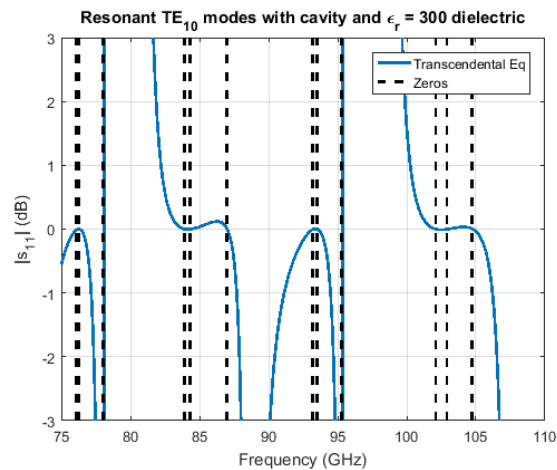


Figure 12: Expected resonances with a measurement setup shown in 11 (a) and a high dielectric constant  $\epsilon_r = 300$ .

## 4 Antenna Concept

The natural antenna to use on a tunable substrate is a microstrip patch antenna - these are resonant antennas which frequency depend on  $\epsilon_r$  of its substrate. A microstrip patch antenna floats above a ground plane allow us to easily DC bias it relative to the ground plane to achieve tunability.

A patch antenna is the most common form, and is typically modeled as a lossy microwave cavity. It has two perfectly conductive boundaries with four magnetic boundaries along the side walls. Dielectric loss of the material will degrade the quality factor of the resonator and ultimately the optical efficiency of the antenna.

A patch antenna concept is shown in figure 13. The optical response of the antenna clearly shifts as a function of dielectric constant, as shown in figure 13b. We use an antenna array design portable to the slot antenna arrays in BICEP/KECK and SPIDER - the number of elements in the array can be adjusted to match the beam width to the telescope optics. A corporate microstrip summing tree coherently sums the signal of the antennas, filter the power, and deposit it onto a TES island.

The simulation shows a unit cell and periodic boundary conditions are enforced. The patch antenna is driven through a slot aperture, which defines the polarization of that antenna. The dielectric used in the simulation is far less than its expected true value - this was done because HFSS is unable to handle dielectrics in the hundreds. Analytic models suggest we simply need to scale the antenna sizes down but further studies are required to understand the simple scaling relations.

The design parameters of the antenna are the geometric dimensions of the patch, the thickness of the substrate on which it is patterned, and the aperture that couples the power to the patch antenna. The geometric factors (length, width of path, and thickness of substrate) along with the dielectric constant determine the frequency of operation. The thickness of the substrate and the aperture transform the patch impedance. Careful design of this would allow us to have a well matched system that allows efficient illumination of the patch with a microstrip mode.

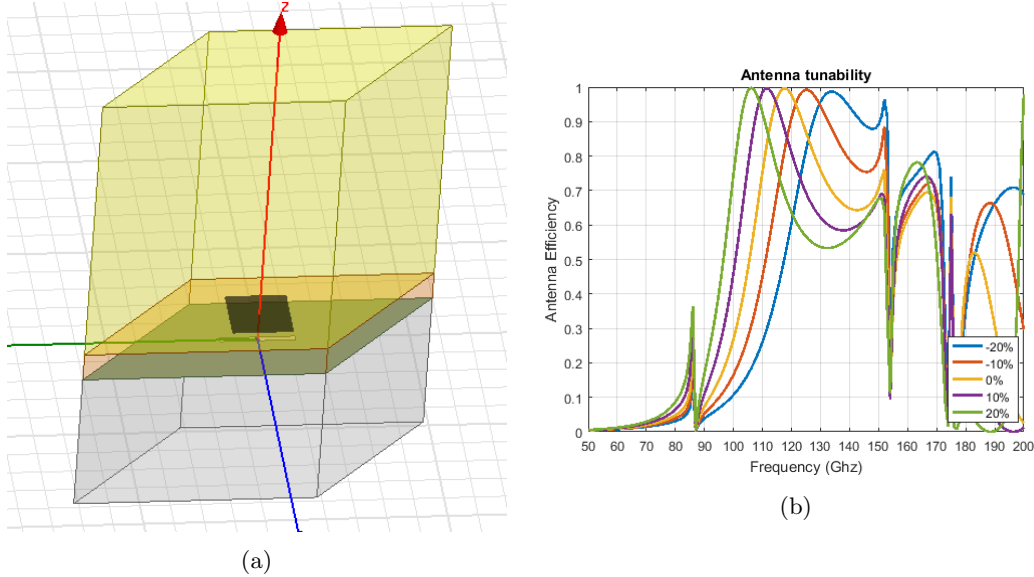


Figure 13: (a) HFSS geometry of an infinite array patch antenna that is driven by a slot. We use a dielectric of  $\epsilon_r = 20$  relatively thick at 0.1mm. The simulation stack up from the top to the bottom is vacuum (yellow), patch, dielectric (orange), ground plane with slot aperture, and silicon (grey). (b) Simulated efficiency of the antenna. We see the frequency response of the antenna is tuned by changing the dielectric constants. Frequencies  $> 150GHz$  show the onset of grating lobes and can be engineered.

## 5 Hardware modifications for a 4K measurement of dielectric properties

We need to pipe signal from the VNA through a small test cryostat. In order to accomplish this, hardware modifications must be made to accommodate the desired setup.

**Machining the resonant cavity** The resonant cavity shown in figure 11 is straight forward to make. We simply can use a commercially produced WR10 waveguide, and create two apertures that will form the resonant cavity. These apertures must be electrically isolated from the cavity to allow for DC-biasing. This can be efficiently accomplished with Kapton tape which is a good isolator, remains sticky under cryogenic temperatures, and is thin (5 mils) which would minimize the perturbation of the cavity.

We machined the waveguide coupling apertures out of 5 mil thick brass shim stock. The template used is shown in figure 14a and allows us to precisely machine the location and size of the coupling aperture.

**Vacuum fittings** In order to pipe signal from an external source to an internal source, we had to modify the IR dewar. We replaced the optical coupling port with a machined vacuum mount. It has an o-ring to form a seal between the piece and the outside of the IR dewar, and a precision machined hole that allows a waveguide vacuum connector piece. The waveguide connector piece is commercially acquired, and has two vacuum tight surfaces: one to form a seal between our vacuum window and the connector piece, and

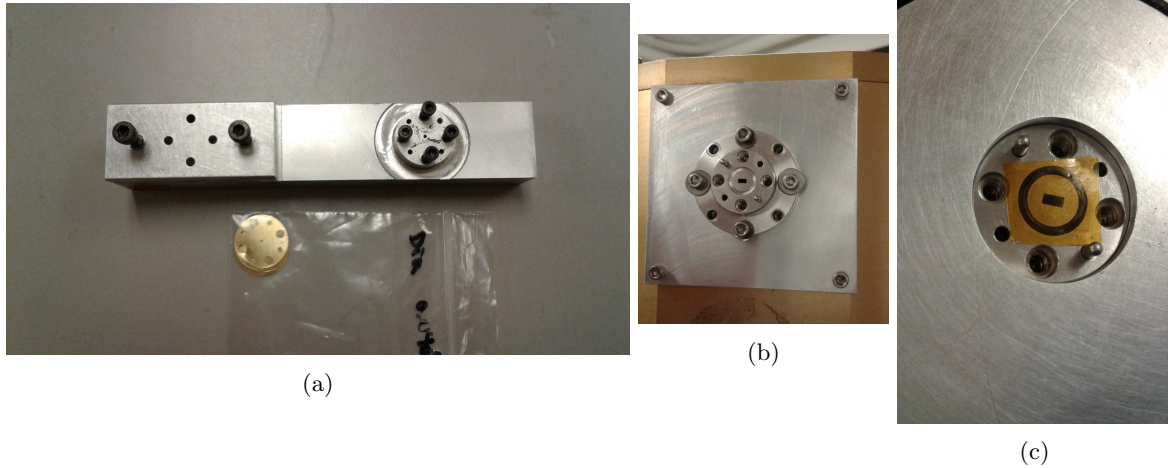


Figure 14: (a) template used to make waveguide apertures from brass shim stock. (b) Vacuum to air waveguide port from the outside (c) to inside. A thin piece of kapton over an o-ring provides a vacuum tight surface.

one to form a seal between the connector piece and another waveguide component. We pumped down on the cryostat using an Agilent Triscroll rough pump, and achieved pressures of  $10^{-2}$  torr within minutes indicating we had a good seal.

**Thermal modeling** It's unavoidable to have a thermal bridge between our 4K stage, where we intend

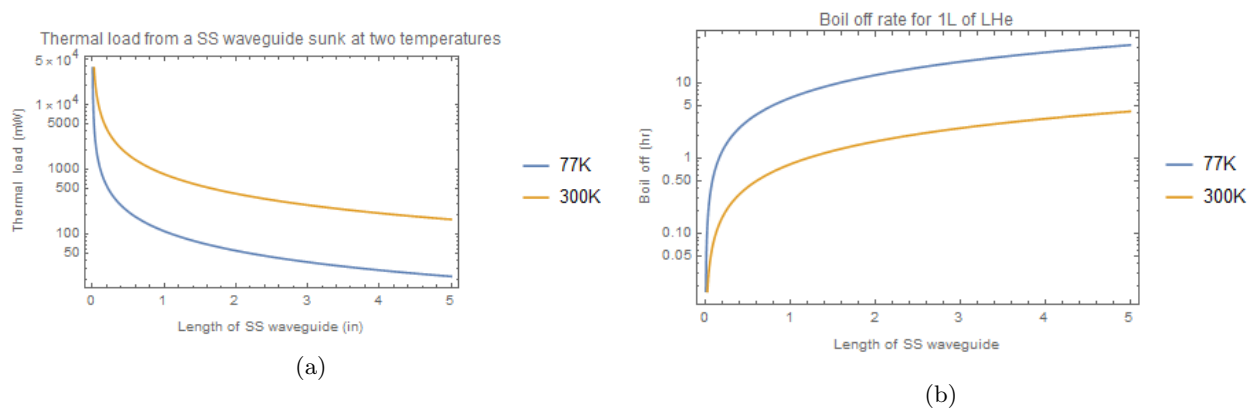


Figure 15: (a) thermal load by a thin-wall (0.020") stainless steel waveguide heat sunk at 77K or 300K. (b) the corresponding boil off rate.

the measurement to occur, and 300K with the vector network analyzer. We have to model the thermal load to ensure that the load is not higher than the cooling power of the stage. We can use a thin wall (.020") stainless steel waveguide to bridge the temperature stages. Assume for simplicity that the thermal drop is precisely across the waveguide and that thermal conductivity is taken the higher of the two stages. For 77K we use  $k \sim 8W/mK$ , and for 300K we use  $k \sim 15W/mK$ , with these values being taken from [2]. We get

figure 15. It takes 2.59kJ of energy to boil of 1L of liquid helium, so we can calculate the boil off rate by this thermal short. We get a reasonable result from using a 2 in thin walled SS waveguide that is not thermally sunk. Such a setup would drop 850mW on the 4K stage. We would boil 1L of LHe in about 50 minutes. Our cryostat can hold 6L of liquid helium, giving margin to do the measurement. A VNA measurement takes several minutes to do a full frequency sweep, so even this rapid boil off would be adequate.

## 6 Future Work

This report takes the first steps towards the developing concept of a tunable antenna. We identified a promising material. We measured its room temperature properties, and we developed the theory behind a high bandwidth method of measuring a high dielectric constant yet still allow the ability to apply an electric field through the material. We also demonstrate the concept of a tunable antenna is sound through simulations, and begun making necessary steps to make a cold-measurement.

To make the cold measurement, we have to dice our STO sample to WR10 dimensions. We have to set up the cryogenics, which potentially could require some effort to debug. 2-3 weeks of dedicated effort would allow us to fully characterize the material property and close the project.

## References

- [1] Robert E. Collin. *Field Theory of Guided Waves*. McGraw-Hill Book Company, 2 edition, 1990.
- [2] J.P. Radebaugh E.D. Marquardt, J. P. Le. Cryogenic material properties database. *11th International Cryocooler Conference*, 2000.
- [3] H. Burkard K. A. Muller. SrTiO<sub>3</sub>: An intrinsic quantum paraelectric below 4 k. *Physical Review B*, 19:3593 – 3603, 1979.
- [4] David Mermin Neil W. Ashcroft. *Solid State Physics*. Brooks Cole, 1 edition, 1976.
- [5] David. M. Pozar. *Microwave Engineering*. John Wiley & Sons, Inc., 4 edition, 2011.
- [6] I. A. Aksay T. Lee. Hierarchical structure - ferroelectricity relationships of barium titanate particles. *Crystal Growth & Design*, 1:401 – 419, 2001.
- [7] I. A. Aksay T. Lee. Quantum paraelectricity probed by superconducting resonators. *Physical Review B*, 95:214513, 2017.